Metallurgical analysis of laser powder bed-fused Al–Si–Mg alloys: Main causes of premature failure

Emanuela Cerri, Emanuele Ghio [*]

University of Parma, Department of Engineering and Architecture, Via G. Usberti 181/A, Italy

A B S T R A C T

AlSi7Mg and AlSi10Mg are the most used alloys to manufacture Laser Powder Bed Fusion lightweight components. These products have high specific strengths but a sometimes-limited ductility. Several direct aging and T6 heat treatments were applied to as-built alloys to solve the problem and optimise their tensile properties. Investigations about causes of premature failure in AlSi7Mg and AlSi10Mg tensile samples were performed in the as-built, direct aged (200°C × 4h) and T6 (solution heat treatment at 505°C × 4h followed by aging at 175°C) treated conditions. In as built and direct aged samples, laser scan track boundaries affected the crack propagation and, consequently, the elongation values in each analysed condition. Higher elongation values were obtained when the crack predominantly propagates within the heat affected zones and along the laser scan track boundaries. After T6 treatment, defects and needle-like δ-Al$_5$FeSi intermetallic particles are observed contributing to the crack nucleation of samples. The laser scan track boundaries remain after the solution heat treatment and redirect the crack propagation in T6 Al-alloys. The effects of precipitation hardened α-Al matrix on the fracture mechanisms were also investigated in AlSi7Mg samples.

1. Introduction

Laser-Powder Bed Fusion (L-PBF) is a relevant additive manufacturing process for the fabrication of Al–Si–Mg components. Its high flexibility, material-saving features, and the possibility to manufacture 3D objects with a complex geometry promote the use of L-PBF in aerospace and automotive applications [1,2]. Industrial sectors, in which the excellent balance between tensile strengths and weight of the Al–Si–Mg alloys, and their corrosion resistance, make them the most used metal alloys [3]. As-built (AB) AlSi7Mg0.6 and AlSi10Mg0.3 alloys generally show higher tensile strengths than the as-cast ones, thanks to their fine microstructure with fine α-Al cells (<1 μm) surrounded by a Si-eutectic network. This network grows with a tubular-like shape from the bottom to the top regions of the sample [4–6]. At the same time, ductility values < 10% conferred by this particular microstructure morphology and by the presence of gas and lack-of-fusion pores can limit the use of Al–Si–Mg components [3,7]. For these reasons, the microstructure morphology and the presence of defects make the analysis of both the failure mechanisms and the consequent damages very important to avoid the premature failure of the manufactured component.

In order to increase the ductility values and to homogenize both the mechanical properties and anisotropy of AB Al–Si–Mg samples, several studies [3,5,8–10] suggested different direct aging (DA) heat treatments at temperatures lower than 225 °C. In fact, DA performed at higher temperatures (>250°C) promotes greater worsening effects on the mechanical properties due to the coarsening phenomena of the Si-eutectic network (a decrease in UTS and YS of – 40% and – 30%, respectively [3]). The best anisotropy reduction and the highest worsening effects on the tensile strength are conferred by the solution heat treatment (SHT). It recrystallizes the α-Al cells into α-Al grains and generates a dispersion of coarsened Si-eutectic particles in the α-Al matrix [3,11]. In this scenario, the damage behavior is substantially controlled by Si-rich particles and not by the Si-eutectic network obviously [12]. As a matter of fact, it depends on the strength, shape, and distribution of secondary phases. Artificial aging (AA) performed on solubilized Al–Si–Mg alloys improves their mechanical properties, at the expense of elongation, through the precipitation hardening of the α-Al matrix. In fact, Petit et al. [13] affirmed that a hardened matrix promotes a void formation at coarse inclusion easier. During artificial or direct aging, Mg and Si alloying elements diffuse from the supersaturated α-Al lattice and harden the α-Al matrix thanks to the following precipitation sequence

Table 1

Nominal chemical compositions (wt.%) of AlSi7Mg and AlSi10Mg powders.

Alloys	Al	Si	Fe	Mg	C	Mn	Cu	O
AlSi7Mg-powder	Bal.	7.04	0.06	0.59	0.007	0.006	<0.005	0.030
AlSi7Mg-sample	Bal.	6.98	0.09	0.58	3.80	–	–	0.60
AlSi10Mg-powder	Bal.	10.0	0.12	0.31	<0.005	0.005	0.001	0.028
AlSi10Mg-sample	Bal.	10.40	0.08	0.28	2.99	–	–	0.52

AlSi7Mg and AlSi10Mg samples were manufactured by L-PBF process into a SLM®280 machine (SLM Solution, Lübeck, Germany) by using the process parameters listed in Table 2.
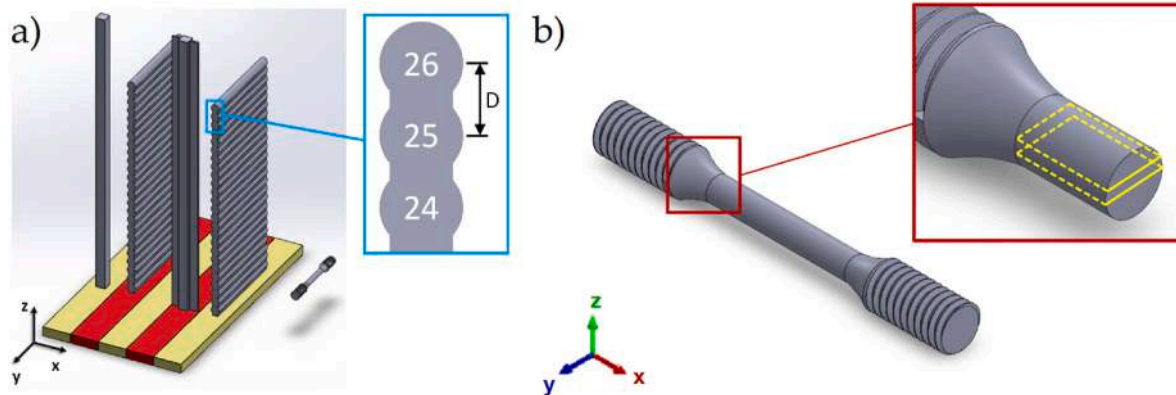

Fig. 1. a) Schematic representation of laser powder bed-fused billets and bars: red and yellow parts indicate the zones in which samples were manufactured through single and double-lasers, respectively. D is about 11.3 mm. b) Tensile sample's geometry after machining process of the billet. Yellow rectangles represent the deposited layer that are parallel to the build platform (xy plane). (For interpretation of the references to colour in this figure legend, the reader is referred to the Web version of this article.)

Table 2

Process parameters used to manufacture AlSi7Mg and AlSi10Mg samples following the skin-core scanning strategy.

Process parameters	Skin	Core
Scanning speed [mm/s]	1400	600
Laser power [W]	370	330
Hatch spacing [μm]	70	
Layer thickness [μm]	90	
Energy density [J/mm^3]	42	87
Build platform temperature [°C]	150	

Table 3

Heat treatment conditions of AlSi7Mg and AlSi10Mg alloys.

Heat Treatments	T, [°C]	t, [h]	Alloys
Direct Aging	200	4	AlSi7Mg, AlSi10Mg
Solution treated	505	4	AlSi7Mg, AlSi10Mg
Solution treated + aging	175	4	AlSi7Mg, AlSi10Mg
		8	AlSi7Mg

[3]: SSS → GP zone → β'' coherent precipitates → β' semi-coherent precipitates → β-Mg$_2$Si incoherent precipitates. The Guinier-Preston (GP) zone consists of a layer of atoms formed by rows of Si and Mg atoms, as analysed by Ref. [14], and it confers the lower strengthening contribution. The metastable β' precipitates confer indeed the highest strengthening effects; while the incoherent β-Mg$_2$Si precipitates lastly confer over-aging phenomena [15,16].

Nevertheless, the technological advances and the optimization of the process parameters, defects like keyhole, gas, and lack-of-fusion (LOF) pores induced by the L-PBF process continue to be a crucial problem in failure mechanism both for AB and heat-treated samples [3,17]. As a matter of fact, crack most likely to propagate along a path with the highest number of defects [18]. In addition, both the precipitation phenomenon and coarsening effects of the gas pores induced by a
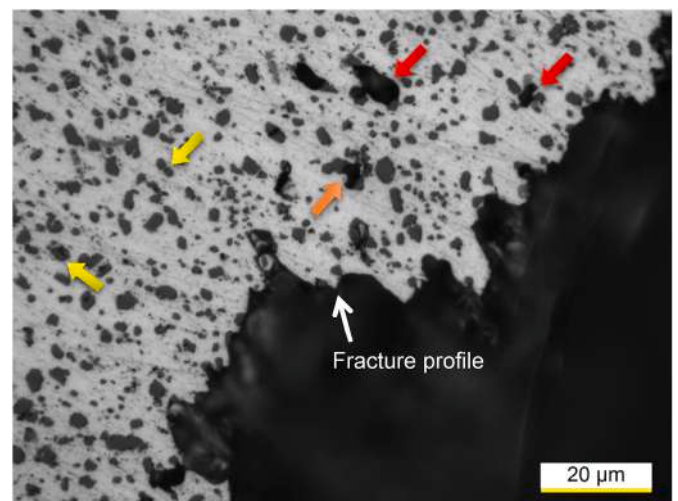

Fig. 2. Representative OM micrograph showing broken Si-particles (yellow arrows), voids formed between two parts of cracked particles (orange one) and formed at Al/Si-eutectic interface (red ones). (For interpretation of the references to colour in this figure legend, the reader is referred to the Web version of this article.)

pre-heated build platform (>150°C) confer another contribution in terms of mechanical properties [5,9,19].

The current investigations aim firstly to describe the failure mechanisms characterizing the AB and heat-treated L-PBF Al–Si–Mg alloys that showed uncharacteristic (unusual or far from average) ductility values. Microstructural analysis and mechanical characterization were already performed in several studies conducted by the authors in Refs. [5,8,9]. Therefore, the paper investigates the correlation between damages taking place during the tensile test at room temperature and the
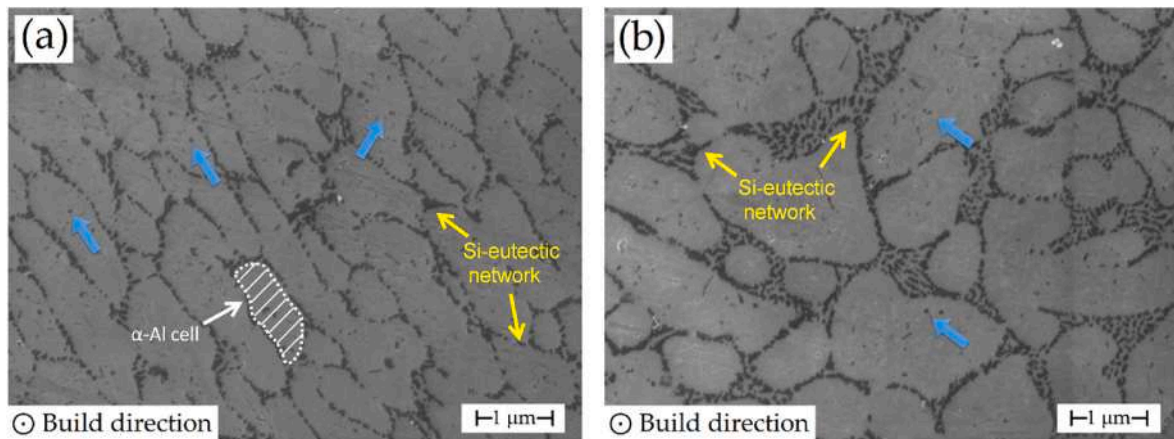
Fig. 3. SEM micrographs of Al–Si–Mg samples in the as-built conditions (xy plane) showing elongated grains aluminum cells in a) and rounded ones in (b). Blue arrows indicate precipitates within the α-Al cells. (For interpretation of the references to colour in this figure legend, the reader is referred to the Web version of this article.)
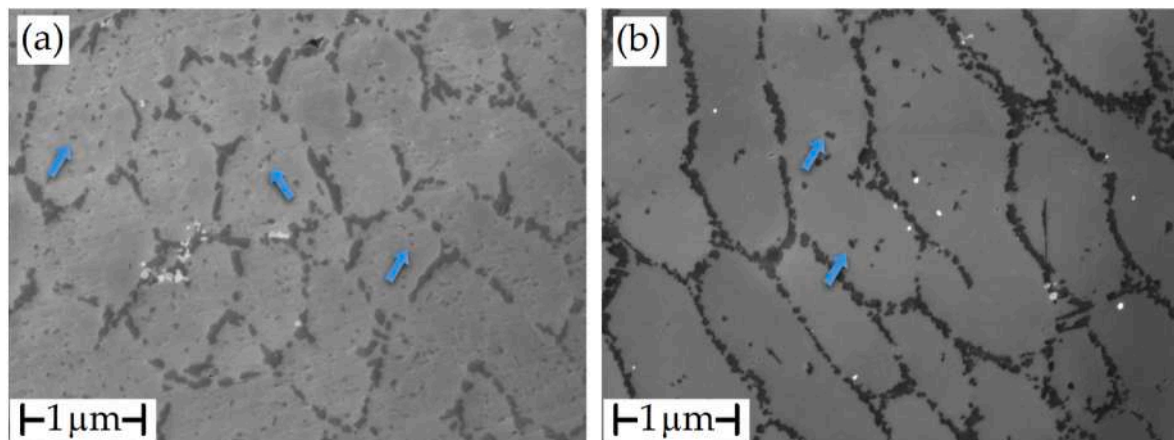

Fig. 4. SEM micrographs of Al–Si–Mg samples of bottom region (a) and top one (b), acquired at 80kX magnification.
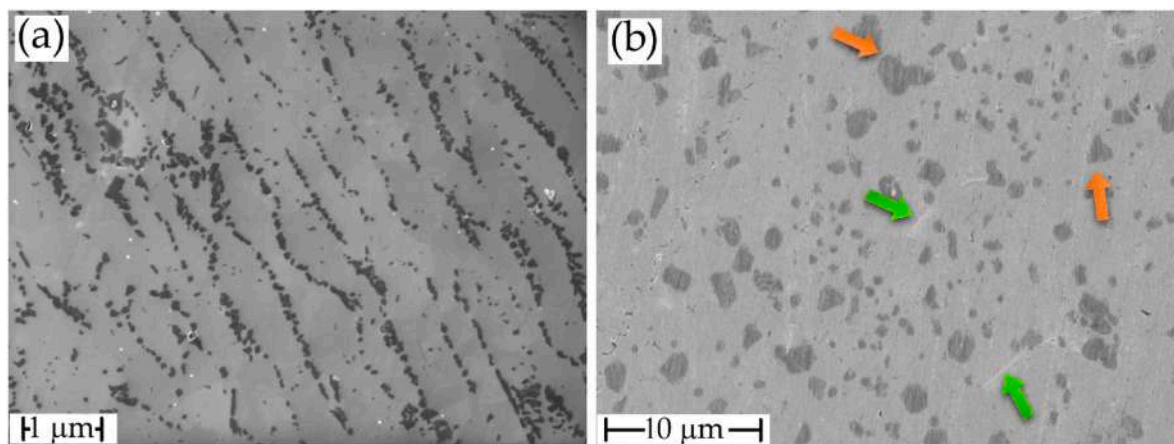

Fig. 5. SEM micrographs of Al–Si–Mg DA at 200 °C × 4 h (a) and after T6 heat treatment (b) acquired at 50kX and 4kX magnifications, respectively. Orange and yellow arrows indicate Si-eutectic particles and Fe-rich intermetallics, respectively. (For interpretation of the references to colour in this figure legend, the reader is referred to the Web version of this article.)

uncharacteristic ductility obtained. Analysis that covers the progressive evolution of the microstructure, in terms of both the Si-eutectic and to α-Al grain growth, from the Si-network (AB) to the globularized and coarsened Si particles (T6). This investigation also explains the causes

that promoted the uncharacteristic ductility values on the same samples by evaluating both the damages induced on the zones very close to fracture surfaces and the fracture morphology. It lastly tries to add relevant findings to the literature in which there is a lack of different
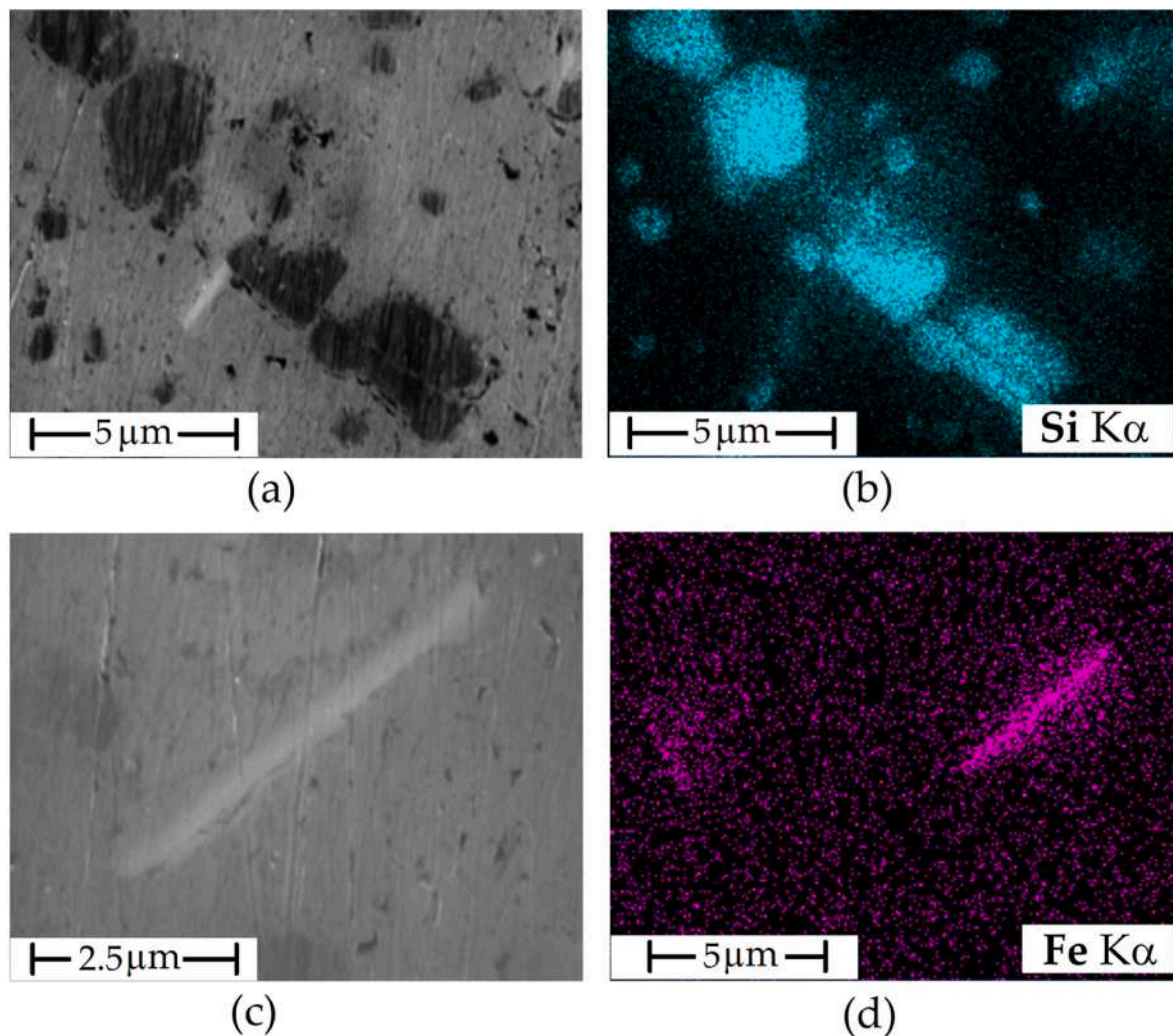
Fig. 6. SEM micrographs and EDS maps showing a) Si particles and b) relative EDS map based on SiKα; c) Fe intermetallic particle and b) relative EDS map based on FeKα.

Table 4
Density values related to AlSi7Mg and AlSi10Mg samples in AB, DA, and T6 conditions.

Heat treatment conditions	AlSi7Mg		AlSi10Mg	
	Top	Bottom	Top	Bottom
As Built	99.87 ± 0.01%	99.88 ± 0.01%	99.83 ± 0.01%	99.87 ± 0.01%
Direct Aging at 200°C-4h	99.89 ± 0.02%	99.62 ± 0.01%	99.60 ± 0.02%	99.73 ± 0.01%
T6 (505°C-4h + 175°C-4h)	99.36 ± 0.01%	98.90 ± 0.04%	98.00 ± 0.03%	98.26 ± 0.04%

aspects of the failure, especially on the damage quantification. Knowing the failure mechanisms of Al–Si–Mg alloys and their damages can provide support for both the design of several AlSi7Mg and AlSi10Mg components and the choice of the best heat treatment.

2. Material and methods

2.1. Materials and L-PBF process

Gas-atomized powders, in the range 20–60 μm, were used to manufacture both AlSi7Mg and AlSi10Mg samples. Their chemical compositions are listed in Table 1. The same table shows the chemical compositions obtained by EDX spectra performed on the AB samples. Higher wt.% contents of C and O were revealed.

Skin-core scan strategy was used to scan and melt each deposited layer. In the core zone, laser scan tracks follow directions inclined of 56.5° with respect to the skin base. The scanning pattern was then rotated of 67° with respect to the previously deposited and scanned layer. For each Al–Si–Mg alloy, more than one billets (base of 100×10 mm^2) and bars (base of 10×10 mm^2) were laser printed perpendicularly to the build platform up to a height of 300 mm (Fig. 1a). Billets were characterized by twenty-six semicylindrical zones from which cylindrical tensile samples were machined (Fig. 1b). For these reasons, the turning process removed the skin zone (depth of ∼ 100 μm) from each sample. Bars were indeed used to obtain the aging profile of AlSi7Mg alloy.

2.2. Mechanical properties

Tensile tests were performed at room temperature using cylindrical-shaped samples (Fig. 1b) according to ASTM E8/E8M standard. Twenty-six tensile samples, with a cross-section area of about (28.5 ± 0.2) mm^2 and a gauge length of 30 mm, were machined by each billet by keeping their major axis of symmetry parallel to the build platform (xy plane in Fig. 1b). For a better understanding of the results, sample '1' is the nearest tensile samples to the pre-heated build platform, while sample
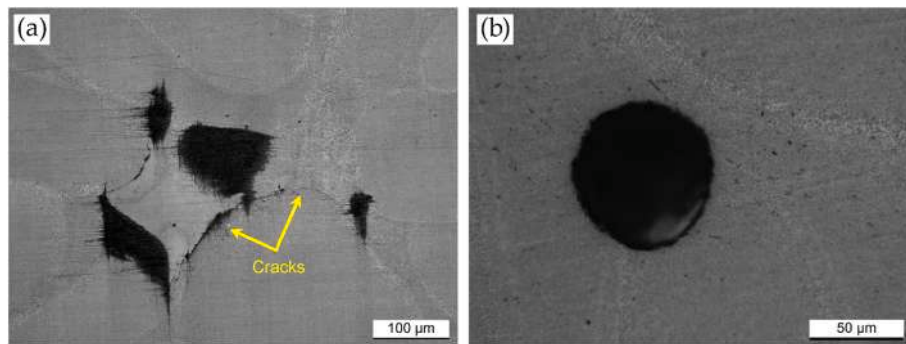
Fig. 7. Lack-of-Fusion (a) and gas (b) pores present in AB Al–Si–Mg samples.
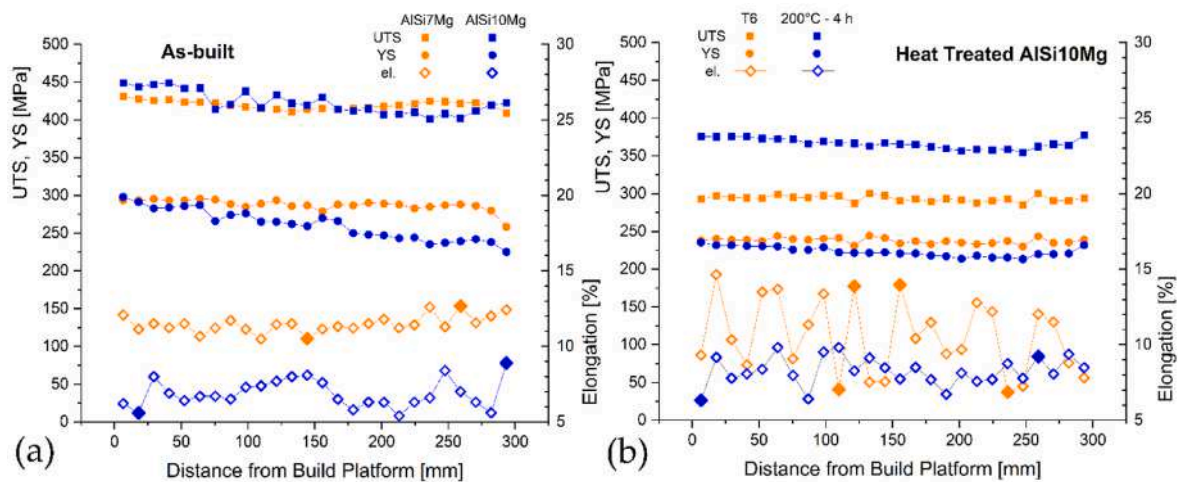

Fig. 8. Mechanical properties of a) As Built samples for both alloys and b) after direct aging at 200°C-4h and T6 treatment (505°C-4h + 175°C-4h) for AlSi10Mg alloy, as function of the distance from the build platform. Elongation data with full symbols belong to samples to be analysed.

Table 5
Minimum and maximum values of elongation related to AlSi7Mg and AlSi10Mg samples.

Alloys	HT conditions	Distance from the building platform [mm]	El. [%]
AlSi7Mg	AB	144.0	10.5
		259.0	12.7
	Solution treated at 505°C-4h	133	22.5
	T6 (505°C-4h + 175°C-4h)	133	10.6
	505°C-4h + 175°C-8h	133	12.2
AlSi10Mg	AB	18	5.6
		295.0	9.1
	DA at 200°C-4h	6.5	9.2
		259	6.5
	T6	110	7.0
		121	13.4
		156	14.0
		271	6.9

Fig. 9. tensile properties and aging curve of AlSi7Mg samples measured after exposure at 505°C – 4 h and at 175 °C (4 h and 8 h).

'26' is the furthest one.

Tensile tests were carried out on AB and heat-treated AlSi7Mg and AlSi10Mg samples (Table 3) using the Z100 (Zwick/Roell, Zwick GmbH, Ulm, Germany) servo-hydraulic machine, with a strain rate of 10^{-2} s^{-1}. Samples were heat-treated before the machining process in a muffle furnace (Nabertherm GmbH, Lilienthal, Germany), where temperatures were controlled by the K-thermocouple placed in contact with the samples. Table 3 lists the heat treatment conditions analysed in the
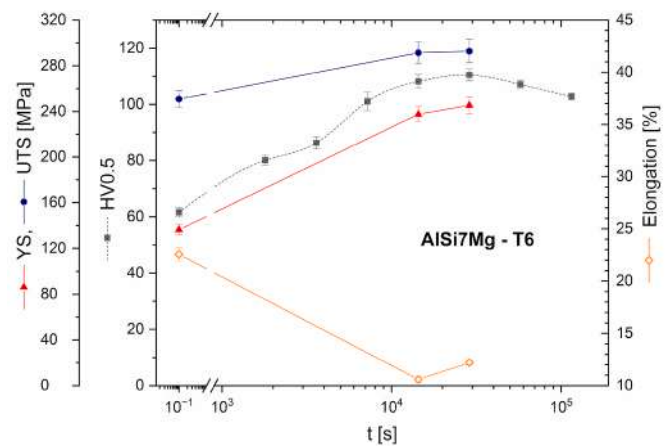
present manuscript which were chosen in relation to the optimization analysis presented and discussed by the authors through the previous studies [5,8,9].

Focusing on AlSi7Mg alloy, the present manuscript also shows the aging curve obtained by treating the solubilized samples (505°C × 4h) at 175°C for exposure time from 0.5 to 32h. Tensile tests were only carried out on samples treated at 8h, since it represents the peak-aging
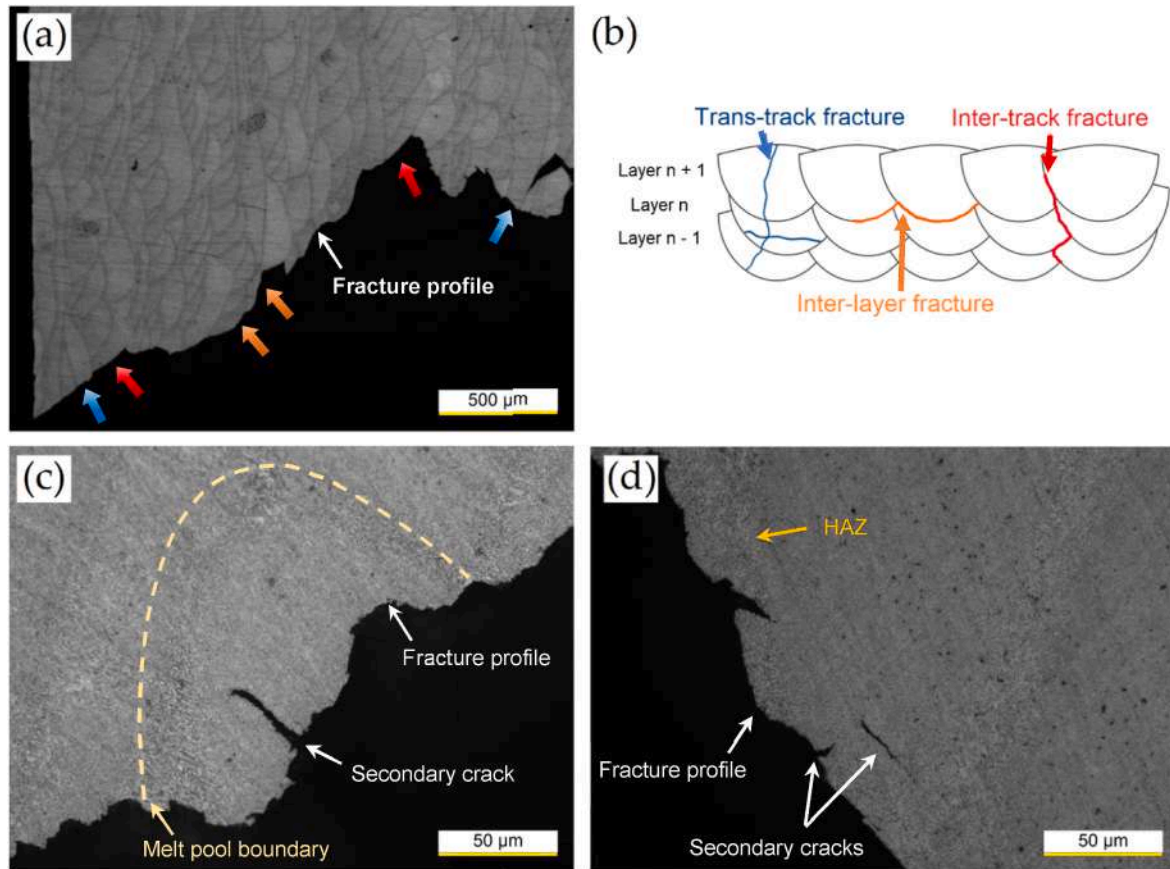
Fig. 10. Fracture profiles of as-built (a) and direct aged (c,d) AlSi10Mg samples, and their possible fracture modes (b) (Adapted from Ref. [3]).

conditions, and at 4h in order to be comparable with T6 AlSi10Mg (505°C × 4h + 175°C × 4h). Aging profiles were obtained by Vickers microhardness measured on ground and polished sample surfaces by applying a load of 500 gf for 15 s. Each HV value was the average of 9 indentations (3x3 matrix).

2.3. Damage analysis

Analyses of fracture profiles were performed through an optical microscope (OM) (DMi8, Leica, Wetzlar, Germany) on polished cross-section area of tensile tested Al–Si–Mg samples. To perform the analyses, each broken sample was divided into two parts by cutting it along the symmetry axis. The mirror-polished surface was obtained with colloidal silica suspensions. The fracture surfaces were, instead, observed through scanning electron microscopy (Auriga Compact FIB-SEM, Zeiss, Oberkochen, Germany), equipped with Schottky Field emitter and EDS microanalysis. Damage of T6 samples was quantified considering i) the % of broken Si-particles (yellow arrows in Fig. 2) and ii) the % of voids formed at Al/Si-eutectic interface (red arrows in Fig. 2) or between two parts of cracked Si-particles (orange arrows in Fig. 2). Light microscopy images were recorded in regions very close to the fracture profile, at a magnification of 1000X for 'i)' and at 200X for 'ii)'. The total population of Si particles was of 1000 objects at least, for each case. The error bands associated with areas of the matrix damages follow the methodology illustrated in Ref. [20]. The percentages of the damaged matrix were lastly calculated.

For a better understanding, "Al–Si–Mg" will be used when AlSi7Mg and AlSi10Mg samples showed the same results unless it is explicitly expressed.

3. Results and discussion

3.1. Microstructure in as-built and heat-treated conditions

Fig. 3 shows SEM micrographs of the as-built microstructure (XY plane) of an Al–Si–Mg sample. The as-built microstructure is characterized by columnar (Fig. 3c) and equiaxed (Fig. 3d) grains present both in the center and at the boundary of the same molten pool. The microstructural difference promotes a variation in terms of strength, hardness, and elongation because the columnar grains better accommodate the crack due to their higher ductility than the equiaxed one [8,9,21]. The α-Al cells, which are surrounded by the Si-eutectic network (yellow arrows in Fig. 3c,d), contain Si nanoparticles (blue arrows) and Mg$_2$Si phases, as confirmed by the authors in Ref. [5] and also supported by Refs. [22–24]. Precipitation phenomena originate from the supersaturated solid solution of the α-Al matrix thanks to the exposure at 150°C (build platform heating) during the fabrication process.

Simultaneously, the different exposure time between the bottom region and the top one promotes a precipitation gradient of Si-nanoparticles (Fig. 4) and Mg$_2$Si phase in the α-Al cells [5]. The bottom region (Fig. 4a) shows indeed a higher number of Si-nanoparticles (blue arrows) than the top one (Fig. 4b). The same exposure time at 150°C influences the sample's density since the bottom regions are characterized by larger pores than the top ones as widely discussed by the authors in Ref. [20]. No variation was observed in terms of the Si-eutectic particle dimensions in the Si-network instead [5,20].

A coarsening phenomenon starts for the Si-eutectic network and Si nanoparticles (Fig. 5a) after exposure at 200°C for 4h, with an average diameter increment of the eutectic Si from (40 ± 10) nm to (60 ± 10) nm. The T6-type heat treatment (505°C-4h plus aging at 175°C-4h) definitely destroys the Si network (Fig. 5b) and the previously nano-
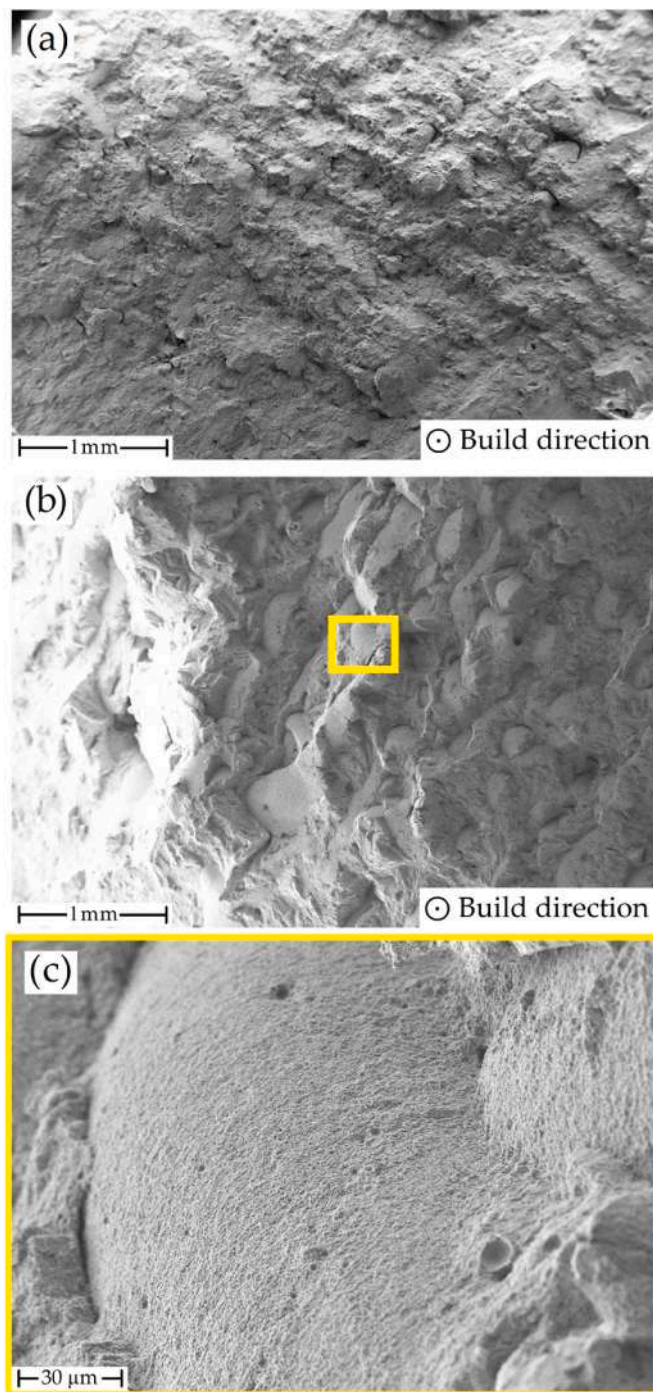
Fig. 11. SEM micrographs of fracture surfaces related to AlSi10Mg samples having minimum (a) and maximum (b) elongations; c) higher magnification micrograph of yellow zone in b). (For interpretation of the references to colour in this figure legend, the reader is referred to the Web version of this article.)

sized α-Al cells become bigger α-Al grains as revealed through the channeling effects exhibited and discussed by the authors in Ref. [20]. Other studies [3,19,25] support these findings. The coarsened si particles have dimensions in the range (0.2–5.4) μm for AlSi7Mg and (0.2–7.4) μm for AlSi10Mg. Particles are more evenly distributed now than in the AB or DA conditions. Fig. 5b also shows needle-like Fe-rich intermetallics (green arrows). Their presence is now visible because of Fe atom diffusion along the grain boundaries or at Al/Si-eutectic interfaces during the exposure at 505°C-4h, as will be confirmed in the figure (Fig. 6).
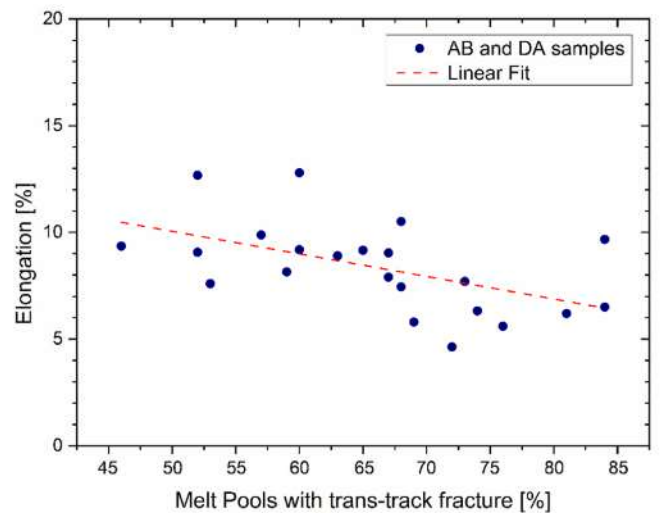

Fig. 12. Elongation values of AB and DA Al–Si–Mg samples correlated to the percentage of cracked laser scan tracks or cracked melt pools (Fig. 10c).

Fig. 6 reports high-magnification SEM micrographs and EDS maps for particle identification. Fig. 6a and 6b refer to coarsened Si particles, with evidence of particle fragmentation and damage, while Fig. 6c and 6d highlight the Fe-rich intermetallic dispersed in the aluminium matrix. In the calculation of damage, Si particles will be taken into consideration.

As the density of the alloys is a property that can be an indication of any problem with the integrity of the material, density values are calculated and listed in Table 4 for different material conditions and heat treatments [20]. Despite the density reduction after exposure at 505°C-4h due to the increase of area and/or number of pores, both AlSi7Mg and AlSi10Mg tensile samples resulted as fully dense samples.

Defects types that affect, firstly, the sample density and, secondly, the crack propagation (as will be discussed later) are the lack-of-fusion 'LOF' (Fig. 7a) and gas pores (Fig. 7b). Several studies analysed the effects of gas and LOF pores to elongation and confirm their influence on the fracture mechanisms in terms of initiation site of micro-crack and preferential path for crack propagation [17,26–28]. Willson-Heid et al. [29] affirmed that pores larger than 450 μm reduce the tensile ductility when the gauge diameter is 6 mm. In this case, LOF pores have more detrimental effects on ductility than gas ones because of their irregular shape, determining high-stress concentration factor at the defect tips [30]. Lastly, Di Egidio et al. [24] affirmed that LOF affects ductility more than microstructural features like grain orientation and size.

3.2. Mechanical properties

Fig. 8a shows the tensile properties of AB AlSi7Mg and AlSi10Mg samples. The UTS and YS values decrease along the height of the build platform due to the precipitation gradient of Si-nanoparticles (Fig. 4) and Mg_2Si [5] promoted by the pre-heated build platform. Previous studies, conducted by the authors, had widely analysed this condition [5,8,9]. At the same time, the % elongation values fluctuate around the average of 12% and 7% for AlSi7Mg and AlSi10Mg, respectively. After T6 heat treatment (505°C-4h + 175°C-4h), UTS and YS of AlSi10Mg become similar from the bottom region to the top one ((293 ± 4) MPa and (238 ± 4) MPa) thanks to the microstructural homogeneity reached in terms of α-Al grains and Si-eutectic particles after the solution heat treatment, and in terms of Mg_2Si precipitates after the artificial aging. Some studies confirmed these observations as also expressed in the Introduction. Ductility values exhibited significant discrepancies ranging between values of 6% and 15%, regardless of their position with respect to the build platform (Fig. 8b) due to the presence of both several
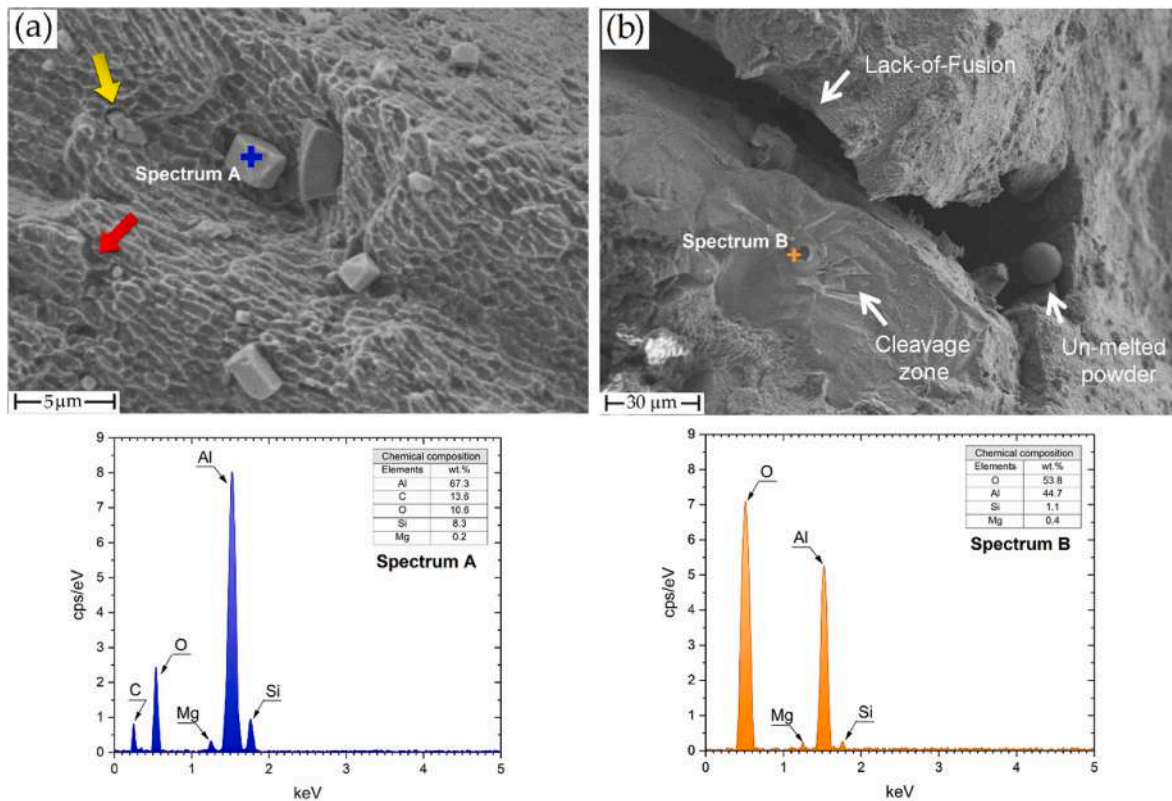
Fig. 13. SEM micrographs of fracture surfaces showing the presence of several defects, such as aluminium carbides (a), aluminium oxides and LOF pore (b). EDS spectra relative to highlighted crosses are shown under each SEM micrograph.
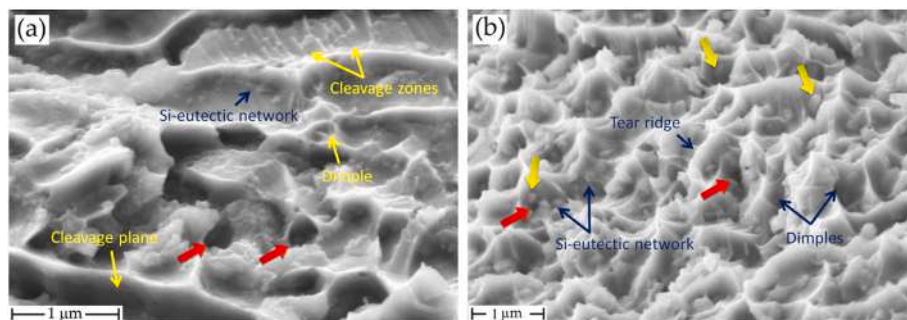

Fig. 14. Fracture surfaces of Al–Si–Mg samples that highlight cleavage zones (a) and tear ridges. Yellow and red arrows indicate Si-particles and matrix damages, respectively. (For interpretation of the references to colour in this figure legend, the reader is referred to the Web version of this article.)

defects, like aluminium oxides and pores, and δ-Al$_5$FeSi phases as will be discussed later. AlSi10Mg samples, DA at 200°C × 4h, are characterized by UTS and YS mean values of (366 ± 7) MPa and (223 ± 6) MPa, respectively, due to the coarsening of both Si-eutectic network and precipitates (Fig. 5a) as investigated by the authors in Ref. [5]. The elongation values also show a fluctuation around an average of 7.5%, regardless of their distance from the build platform. Elongations values identified by the full-coloured symbols in Fig. 8, refer to tensile samples whose longitudinal and tri-dimensional surface fracture will be analysed due to their extreme ductilities (maximum or minimum).

To resume, Table 5 lists the AlSi7Mg and AlSi10Mg samples characterized by minimum and maximum values of elongation, whose fracture surfaces and results will be analysed and discussed in section 3.3.

Fig. 9 shows mechanical test results of AlSi7Mg samples after T6 treatment (505°C-4h + aging at 175°C) which will be subsequently considered for damage evaluation. Vickers microhardness values show a

typical profile of an age-hardening material, with an increase from (62 ± 2) to (111 ± 2) HV0.5 at the peak-aging value. Similar trends were confirmed for the UTS and YS which increased from (163 ± 4) to (245 ± 8) MPa and from (251 ± 7) to (293 ± 10) MPa, respectively. Conversely, % elongation values strongly decreased from (22.5 ± 0.6)% to (10.6 ± 0.3)% after 4h aging of artificial aging at 175°C, and it slightly increased to (12.2 ± 0.2)% at the peak-aging condition. In the latter case, ductility exhibits an unusual trend between 4 and 8h of exposure.

3.3. Fractography

Fig. 10 illustrates the fracture surface profile closest to the middle longitudinal plane of the AlSi10Mg alloy. At low magnification, the same fracture path is visible for AB (Fig. 10a) and DA samples (Fig. 10c, d). The crack generally propagates both in *trans*-track (blue arrows in Fig. 10a,b) and in inter-track (red arrows in Fig. 10a,b) modes, according to other studies in which horizontal samples were investigated
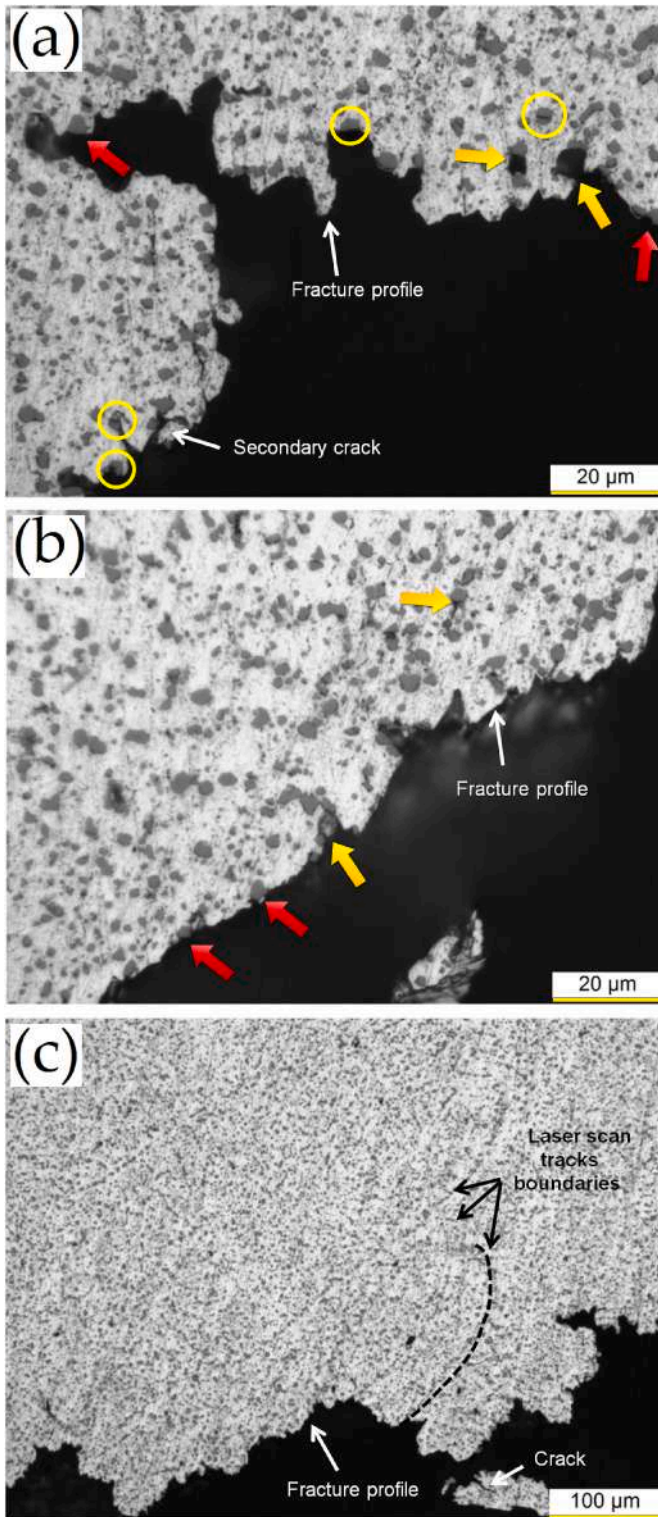
Fig. 15. Fracture profiles of T6 Al–Si–Mg samples having elongation <10% (minimum) (a) and >10% (maximum) (b) elongations. c) Fracture profile of T6 Al–Si–Mg sample showing the influence of several laser scan track boundaries.

[24,31,32]. At the beginning, the crack propagates in *trans*-track mode across the laser scan track or molten pool center (Fig. 10c). Later on, the inter-track or inter-layer zone (orange arrows in Fig. 10b) allows the crack advancement through the HAZ zone (Fig. 10d). The same considerations apply to AlSi7Mg samples.

The fracture surfaces of AB AlSi10Mg samples are illustrated in

Fig. 11. Figs. 11a and 11b compare the *trans*-track and the inter-track propagations of the cracks, respectively, in Al–Si–Mg samples characterized by the minimum (~ 5.6%) and maximum (~ 9.1%) elongation values. The presence of slanted surfaces (Fig. 11a,b) indicates the predominance of shear stress during the fracture process rather than the tensile one. The same observations were made by Refs. [32,33]. These SEM micrographs also highlight the presence of secondary cracks, gas pores, and zones where un-melted powders are partially fused during the L-PBF process that accommodate the propagation of the main crack (Fig. 11c). The crack that propagates into HAZ (inter-layer fracture) makes visible the half-cylindrical shape of the laser scan tracks instead (Fig. 11c). HAZ generally accommodates the crack propagation due to its lower YS than that characterizes the molten pool center [3,5,24]. This condition promotes a higher amount of plastic deformation on HAZ.

Since the *trans*-track fracture mechanism seems to be the primary one, the elongation % has been plotted versus the % of melt pools which exhibit trans track fracture (Fig. 12). The graph in Fig. 12 confirms that less ductile samples (both AB and DA) show cracks that basically propagates in *trans*-track mode (Fig. 10b, c and Fig. 11a). The same conclusions are also drawn by Rosenthal et al. [34]. These results are not always correlated to those of the strengths, since higher elongations sometimes correspond to higher strengths (Fig. 8b) when typically, the reverse should be the case.

A more in-depth investigation shows that the crack path is strongly influenced by the presence of several defects revealed on fracture surfaces of less ductile samples, such as cubic-shaped inclusions in Fig. 13a. The inclusions promote the crack propagation thanks i) to void formation and growth (red arrows in Fig. 13a), ii) to crack initiation sites (yellow arrows in Fig. 13b), due to the developed stress concentrations during the tensile test [35–37]. The origin of these non-metallic inclusions, referable as aluminium carbide thanks to the EDX spectrum A and their cubic-shaped (Fig. 13b), can be traced back to both powder contamination (Table 1) and to the possible problems related to the L-PBF process [38,39]. In both cases, no further analysis can be done on these aspects. Finally, lower ductility values (Fig. 8) were probably affected by aluminium oxides (Fig. 13b) that promote crack initiation and cause a local brittle fracture (cleavage zone) of the material [39].

At higher magnification (Fig. 14a), the fracture surface presents shallow dimples that reflect low ductility and high strength of the material [4,11]. Tear ridges presented in Fig. 14b indicate a more ductile fracture that occurs in Al–Si–Mg samples having maximum elongation values, compared to those exhibiting cleavage planes (Fig. 14a). Several Si-eutectic particles (yellow arrows) are debonded from the α-Al matrix. Crack propagation takes place indeed along the Si-eutectic network because it can easily interconnect the voids formed at Al/Si-eutectic interface. At the same time, the higher stress localized at the crack tip generally induces a rupture of the Si-eutectic network and the detachment along the α-Al cells due to the elastoplastic behaviour of Si and Al phases. Zhao et al. [40] confirmed the same observation and highlighted the presence of some cracks contained in α-Al cells, namely transgranular cracks. In this latter case, Al–Si–Mg samples are characterized by lower ductility values. On the other hand, ductility failure takes place despite non-evident necking formation, as widely analysed in Ref. [8] through the Considère's criterion. In this study, only T6 Al–Si–Mg samples that show elongation % higher than 10% reaching the formation of the neck.

Void formation at Al/Si-eutectic interface is an energetic process and W [J] is the work necessary to create a crack. It is described by the following equation (1):

$$W \propto \gamma_{Al} + \gamma_{Si} - \gamma_{Al/Si} \tag{1}$$

where γ_{Al}, γ_{Si}, and $\gamma_{Al/Si}$ [mN/m] are the surface energies of the α-Al matrix, Si-eutectic particles, and Al/Si-eutectic interface, respectively [8]. Coarse α-Al cells and damaged Si-eutectic network increase the contribution of $\gamma_{Al/Si}$, so reduce the work necessary to nucleate both void
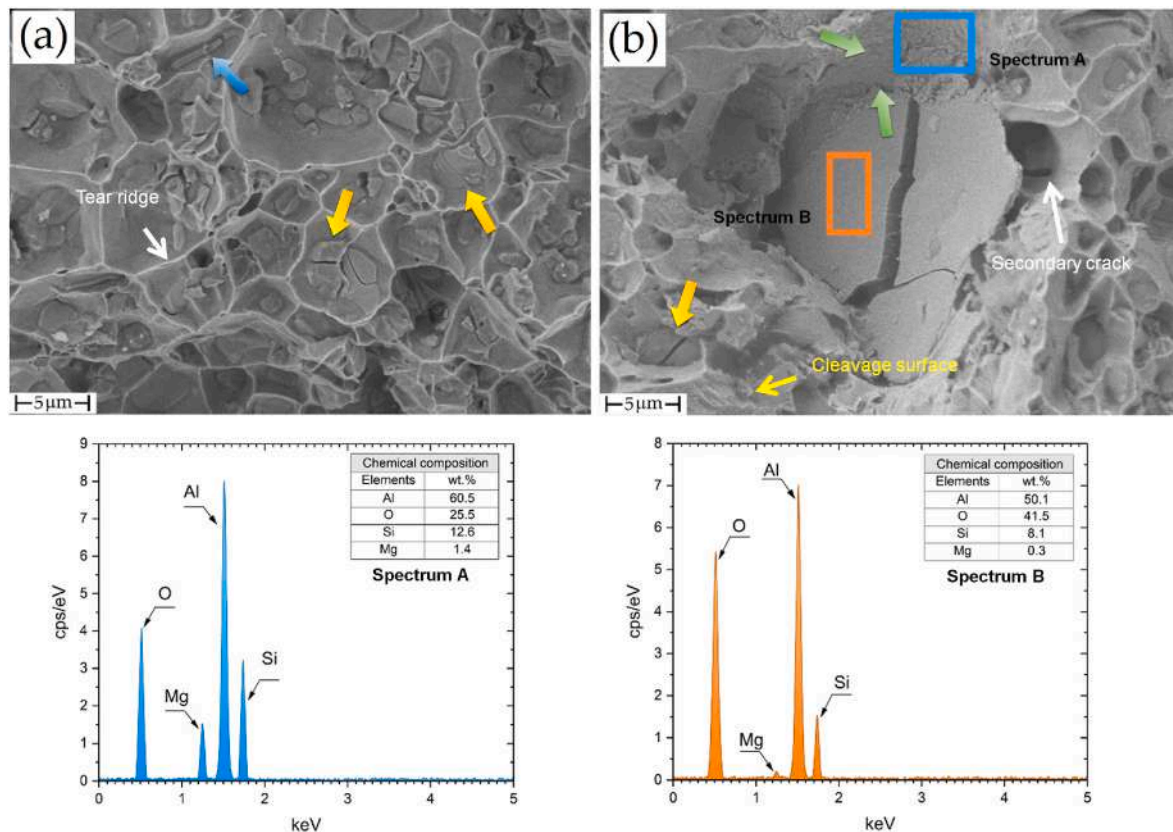
Fig. 16. Fracture surfaces of T6 Al–Si–Mg samples that are characterized by maximum (a) and minimum (b) elongation values. EDX spectra are referred to orange and blue rectangles (d). (For interpretation of the references to colour in this figure legend, the reader is referred to the Web version of this article.)

and crack [40]. This is a condition for which crack propagation is favoured in HAZ in samples where defects do not deflect the crack propagation.

Considering T6 Al–Si–Mg samples (Fig. 15), crack generally propagates by interconnecting the voids formed at Al/Si-eutectic interface (Eq. (1)) and detaches the Si-eutectic particles from the α-Al matrix (red arrows). At the same time, crack can advance through the matrix damages (yellow arrows) or across through cracked Si-eutectic particles (yellow circles). In details, the tortuous crack pathway shown in Fig. 15a characterized T6 Al–Si–Mg samples having elongation <10%, while the more linear one (Fig. 15b) referred to T6 samples with elongation >10%. It is useful to note that fracture mode does not show significant changes from the AB and DA Al–Si–Mg samples since it is based on dimples and microvoid coalescence [24,34]. Voids nucleate at Al/Si-eutectic interface due to Si particle decohesion or fracture, and then voids grow thanks to plastic straining of the close α-Al matrix. Moreover, silicon particle size affects the damage mechanism. Small Si particles generate lower stress concentration than the big ones and contain a lower density of defects which reduces both the probability of void formation and their rupture. Fig. 15a also shows secondary cracks that tend to interconnect bigger Si particles due to their debonding and cracking. Tortuous fracture profile and secondary cracks generally characterized Al–Si–Mg samples with lower ductility values. At the same time, they also show a higher amount of melt pool and laser scan track boundaries, which remain visible even after the SHT, reroute the crack path due to the closeness between the Si-particles (Fig. 15c) [8].

From a 3D point of view (Fig. 16), the fracture surfaces show large Si particles (yellow arrows, Fig. 16a) with one or more brittle cracks due to the critical load transferred by the α-Al matrix [37,41]. Large Si-particles, in fact, contain substantially higher amounts of internal defects increasing the probability of Si-particle failure and void formation ($\gamma_{Al/si}$ in Eq. (1)). At the same time, it needs higher load plastic

deformation at Al/Si-eutectic interface to trigger void nucleation. This is one of the reasons why T6 Al–Si–Mg samples show higher ductility than AB and DA ones. Fig. 16a also shows the presence of a cracked needle-like δ-Al_5FeSi intermetallic (blue arrow) within a dimple. Fig. 15b shows a cracked aluminium oxide (orange spectrum) that may promote the premature failure of the Al–Si–Mg sample together with the LOF defect in which it is located. Green arrows indicate the portion of un-broken α-Al matrix part of the LOF defect on which smaller aluminium oxide particles (blue spectrum) were formed during the L-PBF process. LOF and aluminium oxide particles influence the mechanical behaviour of T6 Al–Si–Mg samples by reducing their ductility values. The fluctuation of % elongation values (Fig. 8) can be also conferred by the increase in the number of pores during the SHT, as widely presented and discussed in Ref. [20].

Focusing on the elongation values of solubilized and aged AlSi7Mg samples (Fig. 9), the percentage of the damaged matrix decreases with ductility (Fig. 17a). As a matter of fact, SHT samples show – 92% and – 78% of the damaged matrix than the aged samples at 8h and 4h, respectively. In addition, the analysed matrix damages in SHT samples are characterized by lower mean area, as reported in Fig. 17b. On the contrary, the hardened α-Al matrix of aged samples confers greater percentages of damages. The precipitation phenomena, responsible for α-Al matrix hardening, promote indeed damage nucleation on coarse particles and its coalescence during the tensile test [13,37,42]. Fig. 17c shows the percentage of broken Si-particles counted in the analysed area close to the fracture profile. The high percentage corresponds proportionally to the lower amount of matrix damages in solution heat treated samples. Therefore, the fracture mechanism is substantially based on the interconnection of both the debonding formed at the Al/Si-eutectic interface and of broken Si-particles. The higher percentage of the damaged matrix (Fig. 17a) corresponds to lower values of broken Si-particle, and vice-versa. In this context, aged samples at 175°C × 4h
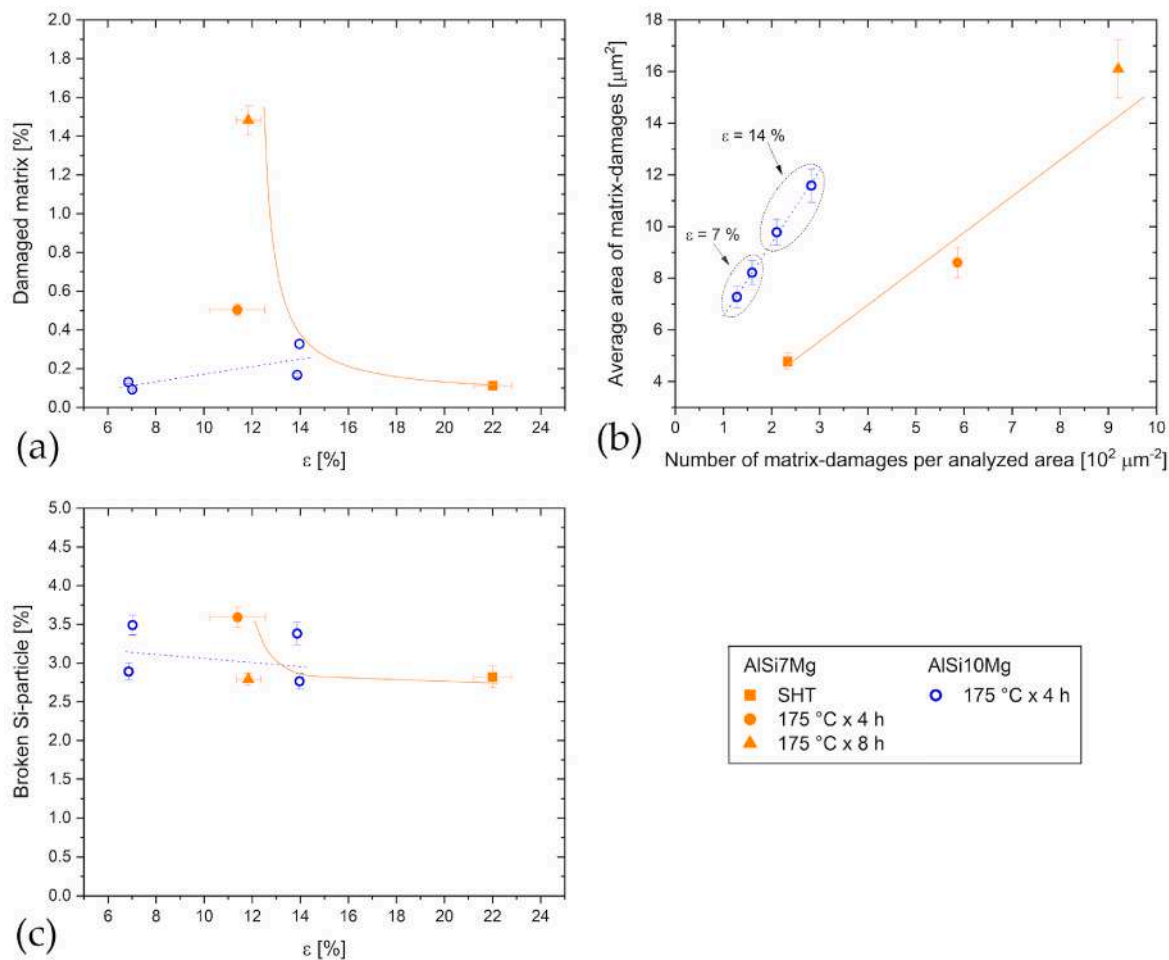
Fig. 17. Results obtained by analysis of AlSi7Mg and AlSi10Mg samples: percentage of the damaged matrix vs. elongation (a), average area of matrix damages vs. the number of damages per analysed area (b) and broken Si-particles vs. elongation (c).

were characterized by a higher debonding phenomenon of Si-particles from the α-Al matrix, while those in peak-aging conditions by cracking phenomena of Si-particles. As a matter of fact, Fig. 17c does not consider the broken Si-particles separated by a damage zone. The most hardened α-Al matrix generates a high amount of dislocation compared to the softer one. The higher stress level reached during the plastic deformation promotes these high amounts of broken Si-particles [13,37]. This fracture behaviour might provide a slight increase in elongation (Δε = 1.6%) shown in Fig. 8. Further analysis of strain hardening effects, and their consequence on ductility behaviour, will be performed through TEM observations. As a matter of fact, differences in terms of size, lattice, and distribution of β'', β', and β precipitates can influence ductility [43,44].

Focusing on AlSi10Mg samples solubilized at 505°C × 4h and aged at 175°C × 4h (peak-aging conditions), the percentage of the damaged matrix increases with elongation values, as shown in Fig. 17a. At the same time, the more ductile samples are characterized by a higher number of damages having large dimensions. Fig. 17c correlates the percentage of broken Si-particles with the elongation. This percentage slightly decreases with the ductility. Samples with a greater percentage of the damaged matrix show a lower percentage of broken Si-particles and vice-versa, as previously discussed for AlSi7Mg alloy. Lastly, the presence of defects and laser scan track boundaries (Figs. 15 and 16) govern the high variation in ductility shown by AlSiMg samples (Table 5).

From the observations previously discussed, Fig. 18 represents the damage mechanism of microstructures that characterize i) AB and DA

samples (Fig. 3 and 5a) and ii) T6 ones (Fig. 5b). When Si-eutectic network form the Al–Si–Mg microstructure, formation of voids takes place on the network due to its load bearing capacity and the consequent dislocation pile-up at the Al/Si-eutectic interface. Once the damage is triggered, the crack quickly interconnects the voids leading to sample failure. This situation explains the presence of the segmented Si-eutectic network (Fig. 15). In a sample devoid of defects (pores, aluminium oxides and/or carbide), cracks generally propagate through the HAZs thanks to their lower failure stress with respect to the center zones of the molten pool [3,24]. The presence of defects, in contrast, can certainly deflect the crack propagation, and can promote the crack initiation due to the stress concentration and consequent void formation (Fig. 13a). More ductile samples show indeed an inter-track mode of fracture, where tear ridges and deeper dimples characterized their fracture surfaces. Cleavage zones (Fig. 14a) and a higher amount of defects (Fig. 15) are indeed observed in the less ductile samples. In the case of T6 samples, the critical load promotes the formation of voids at the Al/Si-eutectic interface and cracked Si-particles (Fig. 15a,b). For the damage based on the Si-particle size, since smaller particles statistically contain less internal defect, they may have higher load capacity (i.e., higher failure stress). Increasing the load, cracks then interconnect Si-broken particles and voids, leading to sample failure. As a result, ductility is reached through void formation, growth, and coalescence. Aluminium oxides and pores can trigger cracks and deflect their propagation lowering the % elongation values. Simultaneously, laser scan tracks (Fig. 16c) influence ductility by deviating the crack propagation thanks to the small inter-particle spacing in their boundaries. Lastly, the
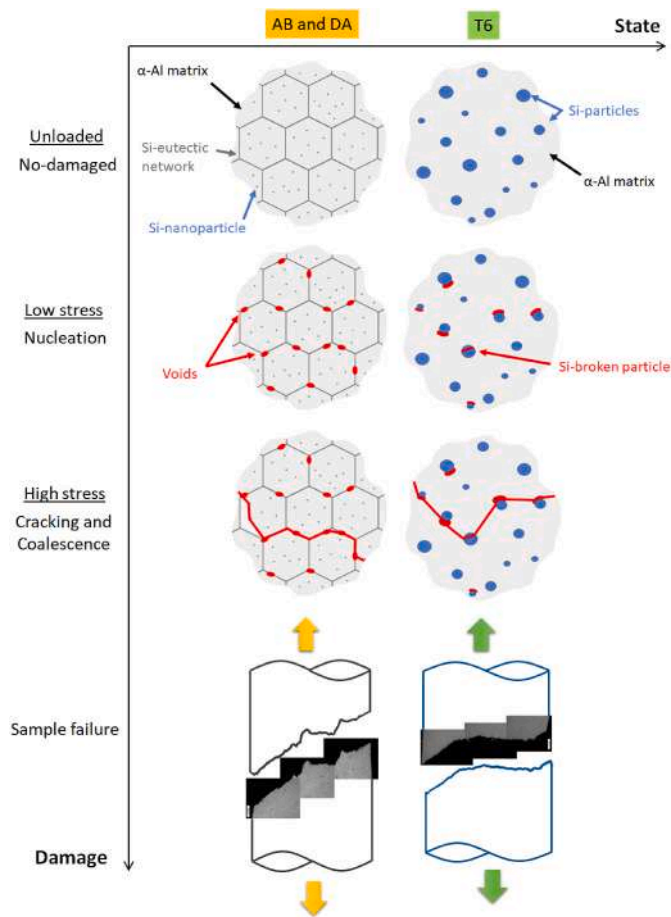
Fig. 18. Schematic representation of the crack propagation in AB, DA, and T6 samples where the main causes of crack initiation and its deflection are illustrated.

formation of voids in the Al-matrix increases with hardening phenomena (Fig. 17).

4. Conclusion

The present manuscript investigated the fracture mechanisms that affect laser powder bed-fused AlSi7Mg and AlSi10Mg samples, and the several causes of their premature failure. Failure analysis carried out on as-built, direct aged at 200°C × 4h, and T6 (SHT at 505°C × 4h followed by AA at 175°C) Al-alloys led to the following conclusions:

1. As-built and direct aged alloys show a local microstructural anisotropy: heat-affected zone generally accommodates the crack propagation because it less effectively hinders the dislocation movement than the melt pool center. In this case, samples show the highest elongation values.
2. As-built and direct aged samples show a combined fracture path: *trans*-track, -layer, and inter-track.
3. Cracks generally nucleate from Al/Si-eutectic interface due to the void nucleation and propagate by interconnecting other formed voids. The presence of several defects (lack-of fusion and gas pores, aluminium oxides and carbides) reroutes the crack propagation, also within the melt pool center, and/or triggers other new cracks. This situation leads to the lowest elongation values and to *trans*-track fracture mechanisms of crack advancement.
4. T6 Al–Si–Mg samples exhibit a fracture mode based on dimples and micro-void coalescence. The presence of defects and/or brittle δ-Al$_5$FeSi phase promotes the crack formation and the consequent

premature failure. Elongation values ($\varepsilon < 10\%$) reach comparable to those obtained by as-built and direct aged samples.
5. The presence of molten pool boundaries in solubilized and T6 Al–Si–Mg samples reroutes the crack paths.
6. SHT AlSi7Mg samples exhibit fracture profiles characterized by deeper dimples than those shown by aged samples. Samples in peak-aged conditions show the highest percentage of the damaged matrix due to both the debonding phenomena at the Al/Si-eutectic interface and the separation of broken Si-particle parts. Aged AlSi7Mg samples show a failure mode governed by both decohesion and particle fracture mechanisms.

CrediT author statement

Emanuela Cerri: Conceptualization, Methodology, Validation, Writing – Original Draft, Writing – Review & Editing, Visualization, Supervision, Project administration, Funding acquisition.
Emanuele Ghio: Conceptualization, Methodology, Data curation, Validation, Investigation, Writing – Original Draft, Writing – Review & Editing, Visualization, Project administration.

Declaration of competing interest

The authors declare that they have no known competing financial interests or personal relationships that could have appeared to influence the work reported in this paper.

Data availability

No data was used for the research described in the article.

Acknowledgements

References

[1] T. Duda, L.V. Raghavan, 3D metal printing technology: the need to re-invent design practice, AI Soc. 33 (2021) 241–252, https://doi.org/10.1007/s00146-018-0809-9.
[2] A. Garcia-Colombo, D. Wood, F. Martina, W. Williams, A comparison framework to support the selection of the best additive manufacturing process for specific aerospace applications, J. Rapid Mater. 9 (2–3) (2020) 194–211, https://doi.org/10.1504/IJRAPIDM.2020.107736.
[3] E. Ghio, E. Cerri, Additive Manufacturing of AlSi10Mg and Ti6Al4V Lightweight alloys via laser powder bed fusion: a review of heat treatments effects, Materials 15 (6) (2022), 2047, https://doi.org/10.3390/ma15062047.
[4] J. Macias, T. Donillard, L. Zhao, E. Maire, G. Pyka, A. Simar, Influence on microstructure, strength and ductility of build platform temperature during laser powder bed fusion of AlSi10Mg, Acta Mater. 201 (2020) 231–243, https://doi.org/10.1016/j.actamat.2020.10.001.
[5] E. Cerri, E. Ghio, G. Bolelli, Effect of distance from build platform and the post-heat treatment of AlSi10Mg alloy manufactured by single and multi-laser SLM, J. Mater. Eng. Perform. 30 (8) (2021) 4981–4992, https://doi.org/10.1007/s11665-021-05577-8.
[6] H. Hyer, L. Zhou, A. Mehta, S. Park, T. Huynh, S. Song, Bai, K. Cho, B. McWilliams, Y. Sohn, Composition-dependent solidification cracking of alluminium-silicon alloys during laser powder bed fusion, Acta Mater. 208 (2021), 116698, https://doi.org/10.1016/j.actamat.2021.116698.
[7] R. Haysen, A study of the effect of porosity content on the ductility of sintered metals, Powder Metall. 20 (1997) 17–20, https://doi.org/10.1179/pom.1997.20.1.17.
[8] E. Ghio, E. Cerri, Work hardening of heat-treated AlSi10Mg alloy manufactured by single and double laser selective laser melting: effects of layer thickness and hatch spacing, Materials 14 (17) (2021) 4901, https://doi.org/10.3390/ma14174901.
[9] E. Cerri, E. Ghio, Aging profiles of AlSi7Mg0.6 and AlSi10Mg0.3 alloys manufactured via laser powder bed fusion: direct aging versus T6, Materials 15 (17) (2022) 6126, https://doi.org/10.3390/ma15176126.
[10] M. Paul, Q. Liu, J. Best, X. Li, J. Kruzic, U. Ramamurty, B. Gludovatz, Fracture resistance of AlSi10Mg fabricated by laser powder bed fusion, Acta Mater. 211 (2021), 116869, https://doi.org/10.1016/j.actamat.2021.116869.

[11] L. Zhao, J. Macias, L. Ding, H. Idrissi, A. Simar, Damage mechanisms in selective laser melted AlSi10Mg under as built and different post-treatment conditions, Mater. Sci. Eng.A 764 (2019), 138210, https://doi.org/10.1016/j.msea.2019.138210.

[12] D. Kim, W. Woo, J. Hwang, K. An, S. Choi, Stress partitioning behavior of an AlSi10Mg alloy produced by selective laser melting during tensile deformation using in situ neutron diffraction, J. Alloys Compd. 686 (2016) 281–286, https://doi.org/10.1016/j.jallcom.2016.06.011.

[13] T. Petit, J. Besson, C. Ritter, K. Colas, L. Helfen, T. Morgeneyer, Effect of hardening on toughness captured by stress-based damage nucleation in 6061 aluminum alloy, Acta Mater. 180 (2019) 349–365, https://doi.org/10.1016/j.actamat.2019.08.055.

[14] G. Thomas, The aging characteristic of aluminium alloys electron transmission studied of Al-Mg-Si alloys, J. Inst. Met. 57 (1961) 90.

[15] Y. Ohmori, L. Doan, Y. Matsuura, S. Kobayashi, K. Nakai, Morphology and crystallography of β-Mg2Si precipitation in Al-Mg-Si alloys, Mater. Trans. 42 (2011) 2576–2583, https://doi.org/10.2320/matertrans.42.2576.

[16] R. Wahi, M. von Heimendahl, On the occurrence of the metastable phase β'' in an Al-Si-Mg alloy, Phys. Status Solidi 24 (1974) 607–612, https://doi.org/10.1002/pssa.2210240228.

[17] C. Laursen, S. DeJog, S. Dickens, A. Exil, D. Susan, J. Carroll, Relationship between ductility and the porosity of additively manufactured AlS10Mg, Mater. Sci. Eng.A 795 (2020), 139922, https://doi.org/10.1016/j.msea.2020.139922.

[18] J. Delahaye, J. Tchuindjang, L. Lecomte-Beckers, O. Rigo, A. Habraken, A. Mertens, Influence of Si precipitates on fracture mechanisms of AlSi10Mg parts processed by Selective Laser Melting, Acta Mater. 175 (2019) 160–170, https://doi.org/10.1016/j.actamat.2019.06.013.

[19] P. Van Cauwenbergh, V. Samaee, L. Thjis, J. N, P. Sedlàk, A. Ivekovic, D. Schyvers, B. Van Hooreweder, K. Vanneensel, Unravelling the multi-scale structure-property relationship of laser powder bed fusion processed and heat-treated AlSi10Mg, Sci. Rep. 11 (2021) 6423–6483, https://doi.org/10.1038/s41598-021-85047-2.

[20] E. Cerri, E. Ghio, G. Bolelli, Defect-correlated Vickers microhardness of Al-Si-Mg alloy manufactured by laser powder bed fusion with post-process heat treatments, J. Mater. Eng. Perform. 31 (2022) 8047–8067, https://doi.org/10.1007/s11665-022-06874-6.

[21] N. Wang, Y. Chen, G. Wu, Q. Zhao, Z. Zhang, L. Zhu, J. Luo, Influence of microstructural heterogeneity on strain partitioning behavior of metals containing columnar grains, Mater. Sci. Eng.A 814 (2021), 141247, https://doi.org/10.1016/j.msea.2021.141247.

[22] J. Li, J. Sun, Y. Li, G. Qian, Z. Wang, Very-high-cycle fatigue induced growth and amorphization of Si particles in additively manufactured AlSi10Mg alloy: dependence of applied stress ratio, Int. J. Fatig. 164 (2022), 107167, https://doi.org/10.1016/j.ijfatigue.2022.107167.

[23] Z. Zhang, J. Li, T. Cheng, Q. Teng, Y. Xie, Y. Wei, W. Li, Simultaneously enhanced strength and ductility of AlSi7Mg alloy fabricated by laser powder bed fusion with on-line static magnetic field, Virtual, Phys. Prototyp. 18 (2023) 17, https://doi.org/10.1080/17452759.2022.2161918.

[24] G. Di Egidio, C. Martini, J. Börjesson, E. Ghassemali, L. Ceschini, A. Morri, Influence of microstructure on fracture mechanisms of the heat-treated AlSi10Mg alloy produced by laser-based powder bed fusion, Materials 16 (5) (2023), https://doi.org/10.3390/ma16052006, 2006.

[25] A. Maamoun, M. Elbestawi, G. Dosbaeva, S. Veldhuis, Thermal post-processing of AlSi10Mg parts produced by Selective Laser Melting using recycled powder, Addit. Manuf. 21 (2018) 234–247, https://doi.org/10.1016/j.addma.2018.03.014.

[26] J. Bao, Z. Wu, S. Wu, D. Hu, W. Sun, R. Wang, The role of defects on tensile deformation and fracture mechanisms of AM AlSi10Mg alloy at room temperature and 250 °C, Eng. Fract. Mech. 261 (2022), 108215, https://doi.org/10.1016/j.engfracmech.2021.108215.

[27] W. Kan, Y. Nadot, M. Foley, L. Ridosz, G. Proust, J. Cairney, Factors that affect the properties of additively-manufactured AlSi10Mg: porosity versus microstructure, Addit. Manuf. 29 (2019), 100805, https://doi.org/10.1016/j.addma.2019.100805.

[28] J. Tiwari, A. Mandal, N. Sathish, A. Agrawal, A. Srivastava, Investigation of porosity, microstructure and mechanical properties of additively manufactured graphene reinforced AlSi10Mg composite, Addit. Manuf. 33 (2020), 101095, https://doi.org/10.1016/j.addma.2020.101095.

[29] A. Wilson-Heid, T. Novak, A. Beese, Characterization of the effects of internal pores on tensile properties of additively manufactured austenitic stainless steel 316L, Exp. Mech. 59 (2019) 793–804, https://doi.org/10.1007/s11340-018-00465-0.

[30] D. Tang, X. He, B. Wu, X. Wang, T. Wang, Y. Li, The effect of porosity defects on the mid-cycle fatigue behavior of directed energy deposited Ti-6Al-4V, Theor. Appl. Fract. Mech. 119 (2022), 103322, https://doi.org/10.1016/j.tafmec.2022.103322.

[31] N. Read, W. Wang, K. Essa, M.M. Attallah, Selective laser melting of AlSi10Mg alloy: process optimization and mechanical properties development, Mater. Des. 65 (2015) 417–424, https://doi.org/10.1016/j.matdes.2014.09.044.

[32] N. Ghisi, H. Ramos, L. Kindleyside, N. Aboulkhair, R. Santiago, The influence of the characteristic microstructure of additively manufactured AlSi10Mg on the plastic behaviour at various strain rates, Mater. Des. 223 (2022), 111112, https://doi.org/10.1016/j.matdes.2022.111112.

[33] M. Aktürk, M. Boy, M. Gupta, S. Waqar, G. Krolczyk, M. Korkmaz, Numerical and experimental investigations of built orientation dependent Johnson–Cook model for selective laser melting manufactured AlSi10Mg, J. Mater. Res. Technol. 15 (2021) 6244–6259, https://doi.org/10.1016/j.jmrt.2021.11.062.

[34] I. Rosenthal, R. Shneck, A. Stern, Heat treatment effect on the mechanical properties and fracture mechanism in AlSi10Mg fabricated by additive manufacturing selective laser melting process, Mater. Sci. Eng.A 729 (2018) 310–322, https://doi.org/10.1016/j.msea.2018.05.074.

[35] A. Rajput, S. Paul, Effect of soft and hard inclusions in tensile deformation and damage mechanism of Aluminum: a molecular dynamics study, J. Alloys Compd. 869 (2021), 159213, https://doi.org/10.1016/j.jallcom.2021.159213.

[36] Y. Chen, S. Pan, M. Zhou, D. Yi, D. Xu, Y. Xu, Effects of inclusions, grain boundaries and grain orientations on the fatigue crack initiation and propagation behavior of 2524-T3 Al alloy, Mater. Sci. Eng.A 580 (2013) 150–158, https://doi.org/10.1016/j.msea.2013.05.053.

[37] D. Broek, The role of inclusions in ductile fracture and fracture toughness, Eng. Fract. Mech. 5 (1973) 55–56, https://doi.org/10.1016/0013-7944(73)90007-6.

[38] S. Matthews, I. Brown, High temperature oxidation of Al4C3, Corrosion Sci. 173 (2020), 108793, https://doi.org/10.1016/j.corsci.2020.108793.

[39] C. Yu, K. Cheng, J. Ding, H. Zhu, C. Deng, C. Bai, Synthesis and some properties of Al4SiC4-Al4O4C composites, Ceram. Int. 44 (2018) 17154–17159, https://doi.org/10.1016/j.ceramint.2018.06.169.

[40] L. Zhao, L. Song, J.G.S. Macìas, Y. Zhu, M. Huang, A. Simar, Z. Li, Review on the correlation between microstructure and mechanical performance for laser powder bed fusion AlSi10Mg, Addit. Manuf. 56 (2022), 102914, https://doi.org/10.1016/j.addma.2022.102914.

[41] L. Babout, Y. Brechet, E. Maire, R. Fougères, On the competition between particle fracture and particle decohesion in metal matrix composites, Acta Mater. 52 (2004), https://doi.org/10.1016/j.actamat.2004.06.009, 4517-1525.

[42] I. Severin, Influence of aging heat-treatment on damage mechanisms of particulate reinforced aluminium matrix composites, Sci. Eng. Compos. Mater. 9 (2000) 25–36, https://doi.org/10.1515/SECM.2000.9.1.25.

[43] S. Megahed, J. Bühring, T. Duffe, A. Bach, K.-U. Schröder, J. Schleifenbaum, Effect of heat treatment on ductility and precipitation size of additively manufactured AlSi10Mg, Metals 12 (8) (2022) 1311, https://doi.org/10.3390/met12081311.

[44] H. Chen, Z. Chen, G. Ji, S. Zhong, H. Wang, A. Borbély, Y. Ke, Y. Bréchet, Experimental and modelling assessment of ductility in a precipitation hardening AlMgScZr alloy, Int. J. Plast. 139 (2021), 102971, https://doi.org/10.1016/j.ijplas.2021.102971.